ACS Energy LETTERS

Open Access

pubs.acs.org/journal/aelccp

Letter

Amorphous $ZrCl_4$-Based Superionic Conductor as a Cost-Effective Solid Electrolyte for Batteries

Guangxing Zhang, Zhantao Liu, Yifan Ma, Jakub Pepas, Hang Xu, Rui Cai, Shuman Xia, Yong Ding, Jianming Bai, Hui Zhong, Yuanzhi Tang,* and Hailong Chen*

Cite This: *ACS Energy Lett.* 2026, 11, 5591−5600

Read Online

ACCESS | Metrics & More | Article Recommendations | Supporting Information

ABSTRACT: Developing highly conductive and cost-effective solid electrolytes is essential for the commercialization of all-solid-state batteries (ASSBs). Zr-based halide electrolytes hold great promise due to their low estimated cost and high oxidation stability. However, the ionic conductivities of most of them are not high enough to enable moderate- and high-rate cycling of ASSBs. Here, fast ion transport is achieved in a group of cost-effective $ZrCl_4$-based electrolytes via a design strategy to create highly disordered amorphous structures. Amorphous $Li_{0.8}ZrCl_4(SO_4)_{0.4}$, with a low estimated cost of \$21 kg^{-1}, achieves an ionic conductivity of 1.86 mS cm^{-1} at 25 °C. It also shows a high oxidation limit of 4.5 V vs Li/Li^+ and good compatibility with high-voltage cathodes, as demonstrated by the stable cycling of ASSBs (73.7% capacity retention after 1000 cycles at 1 C). Synchrotron X-ray diffraction, pair distribution function analysis, and electrochemical impedance spectroscopy reveal that the outstanding conductivity of these amorphous electrolytes is closely related to their short-range and medium-range ordering, revealing new insights for designing high-performance, cost-effective solid electrolytes.

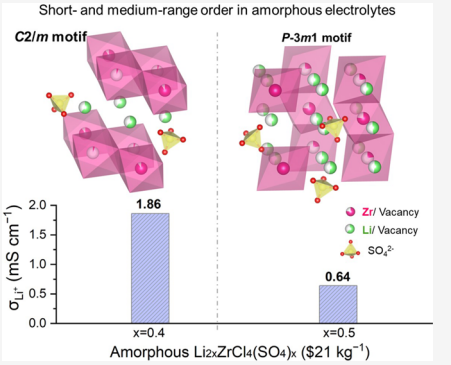

To enable the commercialization of safe and energy-dense all-solid-state batteries (ASSBs), it is essential to develop high-performance solid electrolytes (SEs) that have high ionic conductivity, good deformability, a wide electrochemical stability window, and low cost.[1−4] In recent years, sulfide,[5−8] oxide,[9,10] and halide SEs[11−13] have been extensively studied. However, a single electrolyte that simultaneously meets all these criteria has yet to be identified. Halide SEs with the general formula Li_3MX_6 (M = Y, In, Sc, etc.; X = Cl or Br) show great promise owing to their high ionic conductivity, high oxidation stability (above 4 V vs Li/Li^+), and excellent compressibility.[13−15] In 2018, Asano et al. reported that low-crystalline Li_3YCl_6 exhibits an ionic conductivity of 0.51 mS cm^{-1} at 25 °C and is compatible with uncoated $LiCoO_2$ (LCO).[16] Since then, tremendous efforts have been devoted to developing halide/oxyhalide SEs, such as Li_3InCl_6 (1.49 mS cm^{-1} at 25 °C),[17] Li_3ScCl_6 (3.0 mS cm^{-1} at 25 °C),[18] $Li_2In_{1/3}Sc_{1/3}Cl_4$ (2.0 mS cm^{-1} at 25 °C),[19] $Li_3YCl_3Br_3$ (7.2 mS cm^{-1} at 25 °C),[12] $Li_3GdBr_3Cl_3$ (11 mS cm^{-1} at 25 °C),[13] $LiNbOCl_4$ (12.4 mS cm^{-1} at 25 °C),[20] and $Li_{0.388}Ta_{0.238}La_{0.475}Cl_3$ (3.02 mS cm cm^{-1} at 30 °C).[21] Although high ionic conductivities exceeding 1 mS cm^{-1} have been achieved in these reported halide/oxyhalide SEs, the use of scarce and expensive elements (e.g., Y, Sc, In, Nb, and Ta) poses a major barrier to large-scale commercialization. In comparison, Li_2ZrCl_6 has been reported to be cost-effective, with an estimated cost of approximately \$10 kg^{-1}—well below the \$50 kg^{-1} threshold[22] for large-scale production.[23] However, its limited ionic conductivity of 0.4 mS cm^{-1} calls for further improvements.

Cationic or anionic doping has been attempted to improve the conductivity of Zr halides. For example, aliovalent (Fe^{3+}) doping[24] or oxygen incorporation[25−27] in Li_2ZrCl_6 achieved ionic conductivities of ∼1 mS cm^{-1}. Making SEs in the amorphous phase or disordered states is another promising approach, as demonstrated in some halide SEs.[28−33] Amorphous SEs offer isotropic ionic conduction pathways and less (or no) grain boundaries, which facilitate Li^+ transport and enable high ionic conductivity.[34−36] Despite the absence of long-range structural order, amorphous materials can exhibit short-range order (<5 Å) as well as medium-range order extending to approximately 20 Å. The short-range ordering is closely related to the local coordination environment of the polyhedral building blocks, while the medium-range ordering is related to the spatial arrangement of the polyhedra.[37] Most recent studies have primarily focused on how short-range ordering influences ionic transport in amorphous SEs, while the correlation between medium-range ordering and ionic conductivity

Received: May 1, 2026
Revised: June 4, 2026
Accepted: July 6, 2026
Published: July 28, 2026

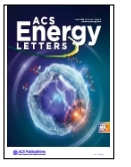

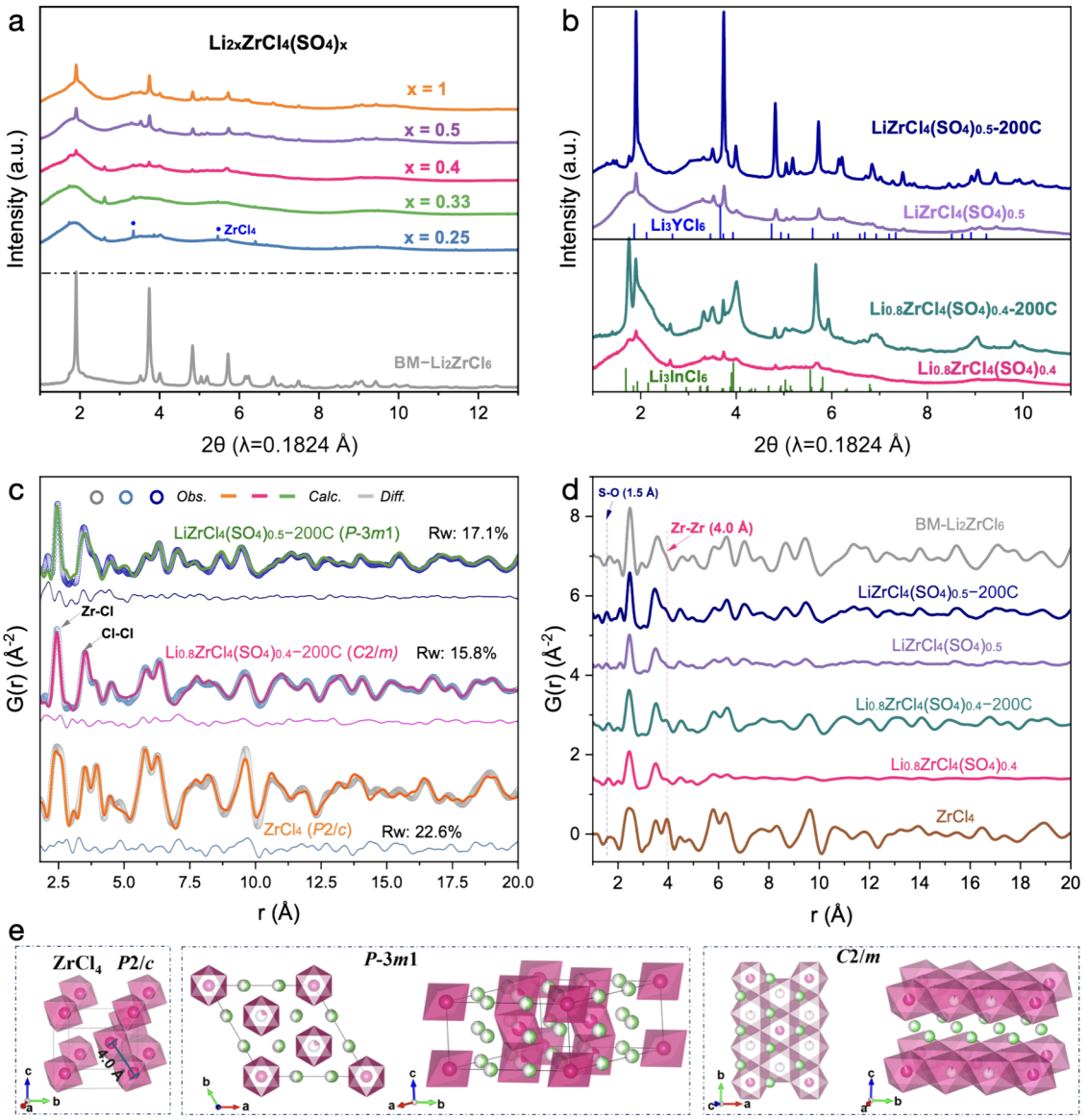

Figure 1. (a) Synchrotron XRD patterns of ball-milled $Li_{2x}ZrCl_4(SO_4)_x$ (x = 0.25, 0.33, 0.4, 0.5, and 1) and Li_2ZrCl_6. (b) Synchrotron XRD patterns of ball-milled $Li_{0.8}ZrCl_4(SO_4)_{0.4}$, 200 °C annealed $Li_{0.8}ZrCl_4(SO_4)_{0.4}$, $LiZrCl_4(SO_4)_{0.5}$, and 200 °C annealed $LiZrCl_4(SO_4)_{0.5}$. (c) PDF $G(r)$ with best-fit for $ZrCl_4$, 200 °C annealed $Li_{0.8}ZrCl_4(SO_4)_{0.4}$, and 200 °C annealed $LiZrCl_4(SO_4)_{0.5}$. (d) PDF $G(r)$ patterns for $ZrCl_4$, ball-milled $Li_{0.8}ZrCl_4(SO_4)_{0.4}$, 200 °C annealed $Li_{0.8}ZrCl_4(SO_4)_{0.4}$, $LiZrCl_4(SO_4)_{0.5}$, 200 °C annealed $LiZrCl_4(SO_4)_{0.5}$, and ball-milled Li_2ZrCl_6. (e) Schematic crystal structures with space groups $P2/c$, $P\bar{3}m1$, and $C2/m$, derived from PDF refinement. Zr and Li are represented by pink and green colored spheres, respectively. The illustrative structures are visualized using VESTA.[40]

remains largely unexplored. Here, we report a series of amorphous $Li_{2x}ZrCl_4(SO_4)_x$ SEs with high ionic conductivities (up to 1.86 mS cm^{-1}) and a very low estimated cost of ~$21 kg^{-1} and discuss the impacts of short-range and medium-range orders on ionic conductivity that are illustrated by synchrotron X-ray diffraction (XRD), pair distribution function (PDF) analysis, and electrochemical characterizations, which provide valuable insights for guiding the rational design of high-performance and low-cost SEs.

A series of amorphous $Li_{2x}ZrCl_4(SO_4)_x$ (x = 0.25, 0.33, 0.4, 0.5, and 1) solid electrolytes were prepared via ball-milling $ZrCl_4$ and Li_2SO_4 with different molar ratios. The synchrotron XRD patterns of ball-milled Li_2ZrCl_6 and $Li_{2x}ZrCl_4(SO_4)_x$ samples are displayed in Figure 1a. Ball-milled Li_2ZrCl_6 (denoted as BM-Li_2ZrCl_6) is used as the baseline material for comparison. It shows sharp Bragg peaks, which can be well-indexed with a $P\bar{3}m1$ space group. As a comparison, ball-milled $Li_{2x}ZrCl_4(SO_4)_x$ samples show majorly broad bumps and only a few relatively sharp peaks, implying a composition of a predominantly amorphous phase with trace crystallites. Quantitative phase analysis based on Rietveld refinement (Figure S1) reveals that these samples contain more than 97 wt % amorphous phases. These findings are further supported by transmission electron microscopy (TEM) observations (Figure S2), where both SAED and HRTEM analyses confirm the predominantly amorphous nature of the samples. In the XRD pattern of $Li_{0.5}ZrCl_4(SO_4)_{0.25}$, a trace amount of residual $ZrCl_4$ can be identified. Upon increasing the Li_2SO_4 ratio to 0.33 in the

https://doi.org/10.1021/acsenergylett.6c01352
ACS Energy Lett. 2026, 11, 5591−5600

starting materials, the $ZrCl_4$ peaks nearly disappear, indicating an almost complete reaction between $ZrCl_4$ and Li_2SO_4. When further increasing the Li_2SO_4 ratio, notably, $LiZrCl_4(SO_4)_{0.5}$ shows different sets of weak and sharp reflections from those observed in $Li_{0.66}ZrCl_4(SO_4)_{0.33}$ and $Li_{0.8}ZrCl_4(SO_4)_{0.4}$, indicating a distinct structure of its crystallites. This variation is likely driven by the higher Li^+ content in the starting materials of $LiZrCl_4(SO_4)_{0.5}$, as evidenced by the observation that $Li_2ZrCl_4(SO_4)$ also displays the same characteristic peaks as $LiZrCl_4(SO_4)_{0.5}$, but with greater intensity.

As the crystalline phases in ball-milled $Li_{2x}ZrCl_4(SO_4)_x$ may be the crystalline phase of the amorphous components,[38,39] we annealed the samples at 200 °C for 3 h to further crystallize the samples to help us interpret the structure of the crystalline and the amorphous phases. Figure 1b compares the synchrotron XRD patterns of the 200 °C-annealed $Li_{2x}ZrCl_4(SO_4)_x$ (x = 0.4 and 0.5, denoted as $Li_{0.8}ZrCl_4(SO_4)_{0.4}$-200C and $LiZrCl_4(SO_4)_{0.5}$-200C, respectively) and the pristine ball-milled counterparts. Upon annealing, the characteristic peaks show enhanced intensity and narrower linewidth without any noticeable shift in peak positions, suggesting that ball-milled samples solely undergo a grain coarsening and crystallization process without a phase transition during annealing. The annealed $Li_{0.8}ZrCl_4(SO_4)_{0.4}$-200C sample is dominated by a monoclinic $C2/m$ phase, isostructural with Li_3InCl_6, whereas $LiZrCl_4(SO_4)_{0.5}$-200C mainly crystallizes in a hexagonal $P\bar{3}m1$ phase similar to Li_3YCl_6, with a minor amorphous component remaining in both samples. The identification of these distinct crystalline phases provides structural references for elucidating the short- to medium-range order of the amorphous component.

To further probe the short- and medium-range order, synchrotron PDF analyses were performed for $Li_{2x}ZrCl_4(SO_4)_x$ (x = 0.4 and 0.5), their annealed counterparts, and $ZrCl_4$ as a reference. The PDF fitting shown in Figure 1c further confirms that $Li_{0.8}ZrCl_4(SO_4)_{0.4}$-200C and $LiZrCl_4(SO_4)_{0.5}$-200C crystallize in the $C2/m$ and $P\bar{3}m1$ space groups, respectively. The schematic crystal structures derived from fitting analysis are illustrated in Figure 1e. Notably, the relatively high Rw values for the two annealed samples may result from the presence of residual sulfate-containing amorphous phases that are not considered in the fitting model. Consistent with the XRD results, the annealed samples are only partially crystallized and still contain an amorphous fraction, which may retain SO_4^{2-} groups. In $ZrCl_4$ ($P2/c$ space group), the $[ZrCl_6]^{2-}$ octahedra share edges to form one-dimensional chains along [001], yielding a prominent Zr–Zr correlation at 4.0 Å. In contrast, the $[ZrCl_6]^{2-}$ octahedra in $C2/m$ and $P\bar{3}m1$ are connected primarily through $[LiCl_6]^{5-}$ or partially occupied $[ZrCl_6]^{2-}$ units, resulting in a much weaker 4.0 Å signal, as shown in Figure 1c. Figure 1d compares the $G(r)$ profiles of ball-milled $Li_{2x}ZrCl_4(SO_4)_x$ (x = 0.4 and 0.5) with those of the reference materials. The PDF $G(r)$ patterns of both ball-milled samples exhibit structural correlations extending up to approximately 10 Å. Beyond this distance, the PDF signals become markedly attenuated, indicating the absence of long-range periodic order. Structural correlations in the 4–10 Å range arise from the spatial arrangement of $[ZrCl_6]^{2-}$ and $[LiCl_6]^{5-}$ octahedra, suggesting the presence of medium-range order. Ball-milled $Li_{0.8}ZrCl_4(SO_4)_{0.4}$ exhibits nearly identical correlations to its annealed counterpart ($C2/m$) up to ~10 Å, demonstrating that its short- and medium-range order closely resembles that of the crystalline phase. Likewise, the amorphous $LiZrCl_4(SO_4)_{0.5}$ retains the same short- and medium-range order, consistent with the crystalline $P\bar{3}m1$ phase. Both are different from the pattern of ball-milled Li_2ZrCl_6, which clearly still has a strong long-range ordering. A distinct peak at ~1.5 Å, attributed to S–O bonds within SO_4^{2-},[36,41] is observed in both amorphous and annealed samples, confirming the incorporation of SO_4^{2-} tetrahedra.

Ionic conductivities of amorphous $Li_{2x}ZrCl_4(SO_4)_x$ samples were measured by electrochemical impedance spectroscopy (EIS) to probe their Li^+ transport properties. The ionic conductivities and corresponding Nyquist plots are shown in Figure 2a and 2b, respectively. BM-Li_2ZrCl_6 possesses an ionic conductivity of 0.35 mS cm^{-1}, which is consistent with previous reports.[23,24] The ionic conductivities of $Li_{2x}ZrCl_4(SO_4)_x$ show a volcanic trend. As the ratio of SO_4^{2-} increases, the ionic conductivity initially increases from 0.85 mS cm^{-1} at x = 0.25 to a maximum of 1.86 mS cm^{-1} at x = 0.4, followed by a decrease to 0.20 mS cm^{-1} at x = 1. The increase in ionic conductivity between x = 0.25 and x = 0.4 is likely due to the increased charge-carrier (Li^+) concentration[1,42] as their structures are quite similar. The decrease of the ionic conductivity, between x = 0.4 and x = 1, however, is likely because those compositions yield different medium- and long-range ordering, as shown in the comparison of the PDF patterns of $Li_{0.8}ZrCl_4(SO_4)_{0.4}$ and $LiZrCl_4(SO_4)_{0.5}$. In ball-milled $Li_{0.8}ZrCl_4(SO_4)_{0.4}$, the long-range ordering is lost, while the medium-range order is retained, which enables a fast local 3D Li^+ diffusion network resembling that in the fully crystallized $C2/m$ structure,[11] contributing to its high ionic conductivity. While for $LiZrCl_4(SO_4)_{0.5}$, although it also loses its long-range ordering and retains the short- and medium-range ordering, its medium-range ordering resembles that in the $P\bar{3}m1$ phase, which is known to be less conductive than the $C2/m$ structure.[16,26] It is thus critical to keep a favorable medium-range ordering for fast Li^+ transport in amorphous solid-state electrolytes.

Additionally, the electronic conductivity of $Li_{0.8}ZrCl_4(SO_4)_{0.4}$ was measured as 3.49×10^{-10} S cm^{-1} via a direct current (DC) polarization method, which is about one order of magnitude lower than that of BM-Li_2ZrCl_6 (2.44×10^{-9} S cm^{-1}) (Figure S3). The high ionic conductivity and low electronic conductivity make it an ideal solid electrolyte. Arrhenius plots of the conductivities of these samples are presented in Figure 2c. The activation energies of the amorphous $Li_{2x}ZrCl_4(SO_4)_x$ samples are all around 0.34 eV, which is lower than many halide and oxide SEs and offers high ionic conductivity at low temperatures.[43] Cyclic voltammetry (CV) tests were performed to assess the electrochemical stability window of amorphous $Li_{0.8}ZrCl_4(SO_4)_{0.4}$ and BM-Li_2ZrCl_6. BM-Li_2ZrCl_6 exhibits an oxidation peak around 3.9 V in the first cycle. By contrast, amorphous $Li_{0.8}ZrCl_4(SO_4)_{0.4}$ shows negligible oxidation currents up to 4.5 V vs Li/Li^+, suggesting excellent oxidation stability and good compatibility with high-voltage cathodes.

The abundance of Zr in Earth's crust is ~165 ppm, which is one to two orders of magnitude higher than that of other metals commonly employed in halide SEs, such as Y, In, Sc, and Nb (Figure 2e). As shown by the estimated bulk prices in Figure 2f, amorphous $Li_{0.8}ZrCl_4(SO_4)_{0.4}$ has a projected cost of \$21 kg^{-1}, primarily due to its low-cost raw materials Li_2SO_4 and $ZrCl_4$, as detailed in Tables S3–S6. It is widely accepted that practical ASSB cells capable of moderate- to high-rate cycling require room-temperature conductivities of the SE to

https://doi.org/10.1021/acsenergylett.6c01352
ACS Energy Lett. 2026, 11, 5591−5600

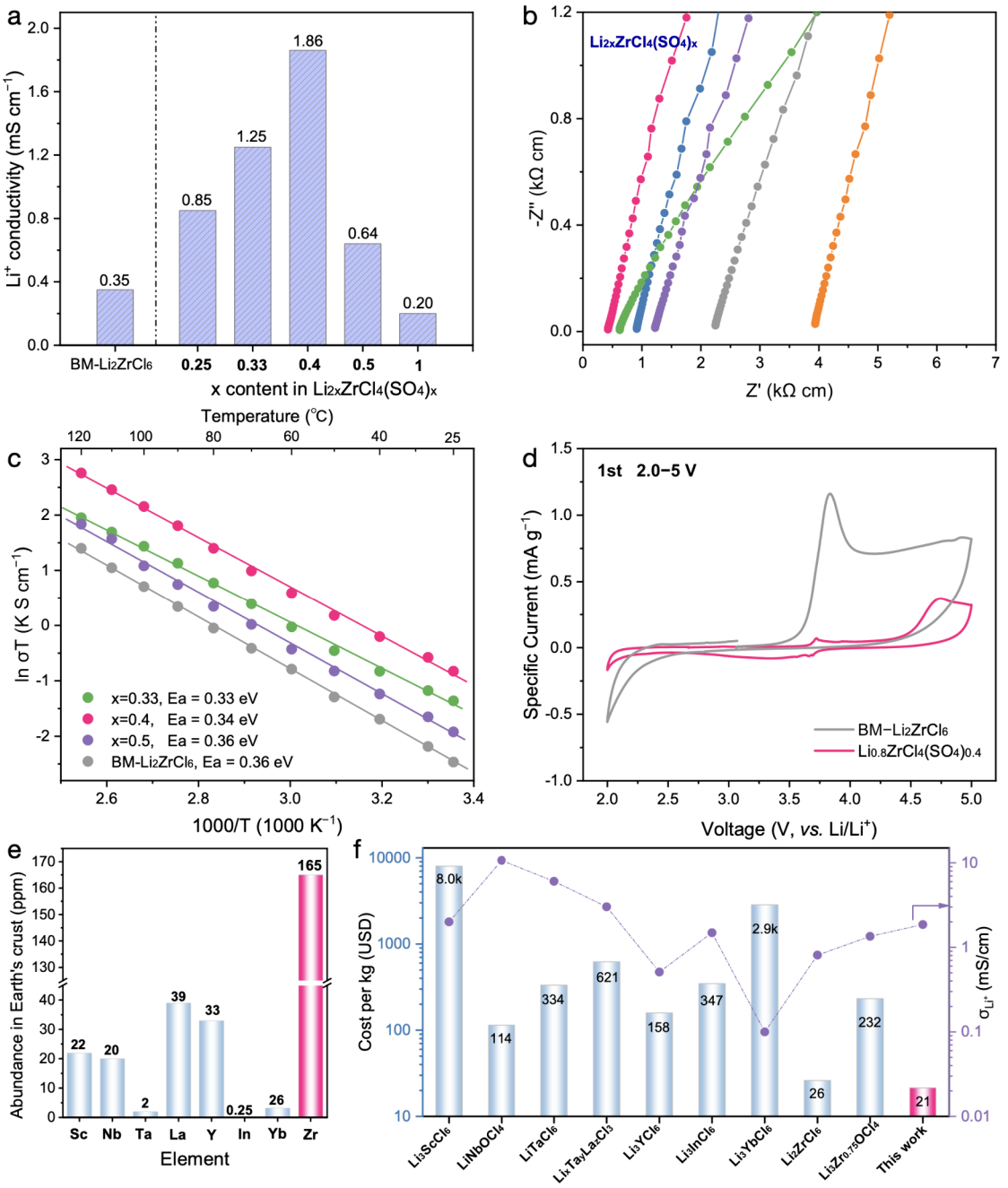

Figure 2. (a) Ionic conductivity and (b) Nyquist plots of ball-milled $Li_{2x}ZrCl_4(SO_4)_x$ (x = 0.25, 0.33, 0.4, 0.5, and 1) and Li_2ZrCl_6, plotted in resistivity form. (c) Arrhenius plots of ball-milled $Li_{2x}ZrCl_4(SO_4)_x$ (x = 0.33, 0.4, and 0.5) and Li_2ZrCl_6. (d) Cyclic voltammogram (CV) curves of ball-milled $Li_{0.8}ZrCl_4(SO_4)_{0.4}$ and Li_2ZrCl_6 with the scan rate of 0.1 mV/s. CV measurements were performed on the Li-In|Li_6PS_5Cl|SE|SE + C cells. (e) Earth's crust abundance of transition metal elements commonly used in halide solid electrolytes. (f) Estimated cost of various halide solid electrolytes when purchased in quantities of 1000 kg (estimated cost based on raw materials only). The bulk prices shown here are also listed in Table S2, while the laboratory-scale prices used to estimate these bulk prices are provided in Tables S3–S6. The reported ionic conductivities of these solid electrolytes are also plotted for comparison.

be at least 1 mS cm^{-1}.[25] Although several previously reported high-performance SEs, such as $LiNbOCl_4$ and $LiTaCl_6$, exhibit outstanding ionic conductivities (~10 mS cm^{-1}),[20,29] they suffer from prohibitively high costs, reaching hundreds or thousands of dollars per kilogram. In contrast, amorphous $Li_{0.8}ZrCl_4(SO_4)_{0.4}$ delivers a high ionic conductivity of 1.86 mS cm^{-1}, exceeding the practical threshold of 1 mS cm^{-1}, while maintaining a low cost that is two orders of magnitude lower. This compelling combination of high ionic conductivity, low cost, high elemental abundance, and minimum supply risks underscores its strong potential for commercial solid-state electrolyte applications.

To further understand the local structure of amorphous $Li_{0.8}ZrCl_4(SO_4)_{0.4}$, X-ray absorption spectroscopy (XAS) and varied-temperature XRD/PDF techniques were conducted. Figure 3a presents the normalized Zr K-edge X-ray absorption

https://doi.org/10.1021/acsenergylett.6c01352
ACS Energy Lett. 2026, 11, 5591−5600

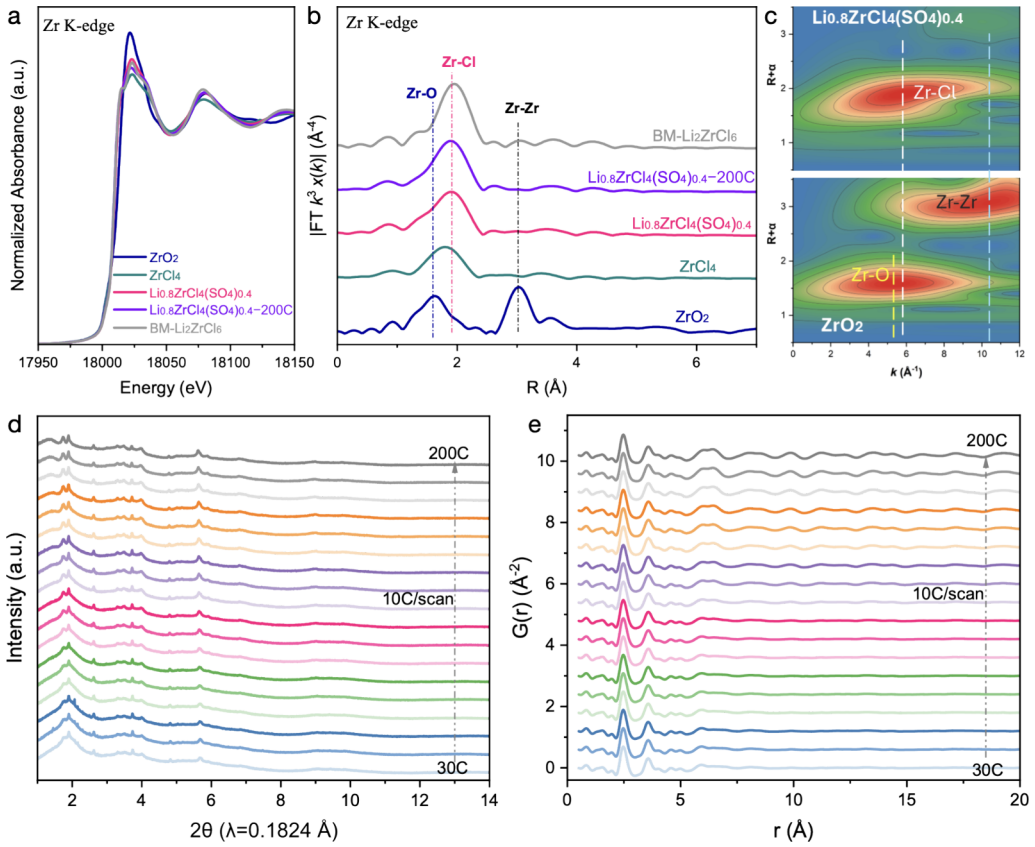

Figure 3. (a) Ex situ XANES and (b) corresponding k^3-weighted Fourier transform EXAFS spectra of ZrO_2, $ZrCl_4$, ball-milled $Li_{0.8}ZrCl_4(SO_4)_{0.4}$, $Li_{0.8}ZrCl_4(SO_4)_{0.4}$-200C, and Li_2ZrCl_6 at the Zr K-edge. (c) k^3-weighted wavelet transforms for the Zr K-edge EXAFS signals of ZrO_2 and ball-milled $Li_{0.8}ZrCl_4(SO_4)_{0.4}$. (d) In situ XRD patterns of ball-milled $Li_{0.8}ZrCl_4(SO_4)_{0.4}$ heated to temperatures ranging from 30–200 °C under an Ar atmosphere, suggesting the crystallization of ball-milled sample to the $C2/m$ structure. (e) In situ PDF $G(r)$ signals of ball-milled $Li_{0.8}ZrCl_4(SO_4)_{0.4}$ heated to temperatures ranging from 30–200 °C under an Ar atmosphere, indicating only the change of long-range ordering.

near-edge structure (XANES) spectra of different samples. The edge position of the reference $ZrCl_4$, determined by the first derivative of the normalized absorption spectrum,[44] is located at 18,010 eV (Figure S4). Amorphous $Li_{0.8}ZrCl_4(SO_4)_{0.4}$, $Li_{0.8}ZrCl_4(SO_4)_{0.4}$-200C, and BM-$Li_2ZrCl_6$ exhibit edge positions identical to that of $ZrCl_4$, indicating a tetravalent oxidation state of Zr in all synthesized samples. The Fourier transformed (FT) extended X-ray absorption fine structure (EXAFS) spectra of all samples are compared in Figure 3b to illustrate the local Zr coordination structure of amorphous $Li_{0.8}ZrCl_4(SO_4)_{0.4}$. Based on the refinement results in Figure S5 and Table S7, peaks at 1.5 and 3.0 Å in the reference ZrO_2 are attributed to the Zr–O and Zr–Zr coordination, respectively. Reference $ZrCl_4$ and BM-Li_2ZrCl_6 exhibit only a peak at ∼1.9 Å, which corresponds to the Zr–Cl coordination.[24] It is worth noting that deviations exist between these FT peak positions and the actual interatomic distances due to phase shift.[45] The Zr–Cl bond length obtained from EXAFS fitting analysis (Table S7) is 2.46 Å, which aligns well with our PDF measurement. Amorphous $Li_{0.8}ZrCl_4(SO_4)_{0.4}$ shows only an asymmetric peak at 1.9 Å with a very weak shoulder near 1.5 Å, suggesting an octahedral $[ZrCl_6]^{2-}$ coordination environment with minor substitution of Cl by O. In a previous report, for O-doped $Li_{x+2y}ZrCl_{4+x}O_y$ SE, O from the starting material Li_2O tends to react with $ZrCl_4$ to form ZrO_2 and preferentially substitutes Cl atoms in the $[ZrCl_6]^{2-}$ octahedra, leading to strong peaks at 1.5 and 3.0 Å.[25,27] The weak shoulder near 1.5 Å observed in our amorphous $Li_{0.8}ZrCl_4(SO_4)_{0.4}$ suggests the stable presence of SO_4^{2-} anions and their interaction with $[ZrCl_6]^{2-}$ octahedra, i.e., some of the $[ZrCl_6]^{2-}$ octahedra and SO_4^{2-} tetrahedra are connected through a shared corner O atom, which replaces one of the six Cl atoms in the $[ZrCl_6]^{2-}$ octahedron. The k^3-weighted wavelet transforms (WT) analysis of the Zr EXAFS signals in Figure 3c further confirms the minor Cl–to–O substitution in the $[ZrCl_6]^{2-}$ octahedron and the absence of ZrO_2.

The medium-range order of amorphous $Li_{0.8}ZrCl_4(SO_4)_{0.4}$ has been shown to resemble that of its annealed counterpart (space group $C2/m$) by the comparison of their PDF patterns. Here, variable-temperature XRD and PDF were used to probe the crystallization and evolution of the medium-range ordering of amorphous $Li_{0.8}ZrCl_4(SO_4)_{0.4}$ upon heating. Synchrotron XRD and PDF data were collected at 10 °C intervals during heating from 30 to 200 °C. Figure 3d shows the in situ synchrotron XRD patterns of amorphous $Li_{0.8}ZrCl_4(SO_4)_{0.4}$ during heating. As the temperature increases, the broad diffraction peak at ∼2 Å becomes sharper, especially after 150 °C. Simultaneously, more characteristic peaks appear, which can be matched to the $C2/m$ space group. The corresponding PDF $G(r)$ profiles in Figure 3e show that medium-range order becomes stronger with heating, indicating the enhancement of medium-range ordering. In contrast, the peaks within 7 Å remain unchanged throughout the heating process, showing

https://doi.org/10.1021/acsenergylett.6c01352
ACS Energy Lett. 2026, 11, 5591−5600

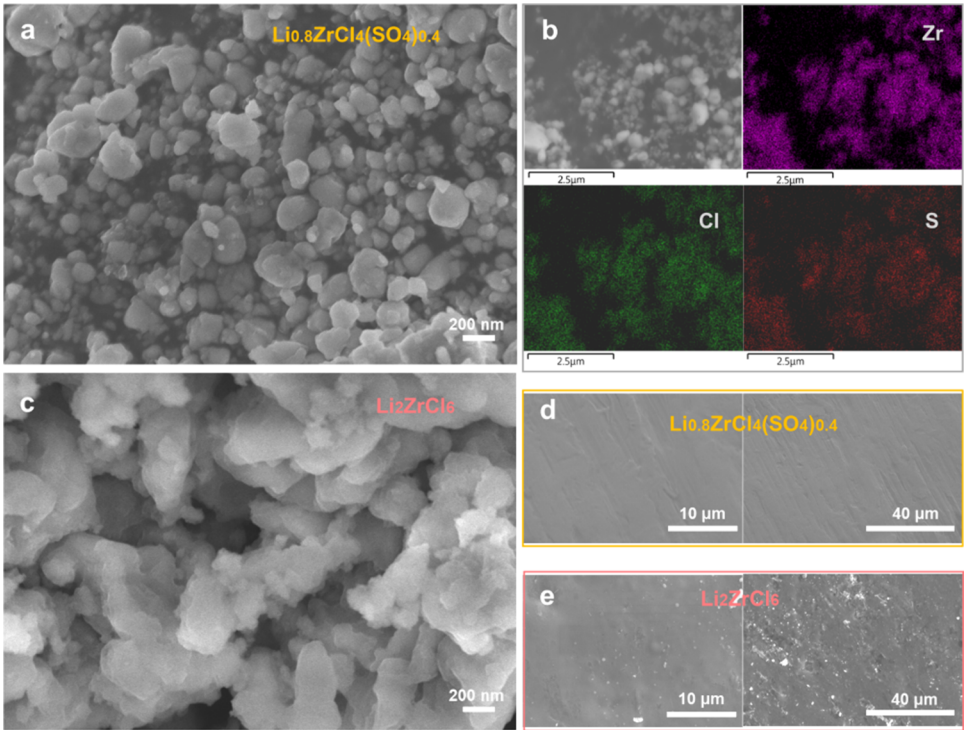

Figure 4. (a) SEM image and (b) EDS elemental mapping of ball-milled $Li_{0.8}ZrCl_4(SO_4)_{0.4}$. (c) SEM image of ball-milled Li_2ZrCl_6. SEM images with low and high magnifications for the cold-pressed pellets of (d) ball-milled $Li_{0.8}ZrCl_4(SO_4)_{0.4}$ and (e) ball-milled Li_2ZrCl_6. All the pellets were fabricated under 243 MPa.

that the local arrangements remain unchanged during crystallization. This confirms that the amorphous material shares a similar short- and medium-range order with the structural motif of the *C*2/*m* phase.

The morphology and deformability of amorphous $Li_{0.8}ZrCl_4(SO_4)_{0.4}$ were characterized as well. As reported by Shi et al.,[46] smaller solid-electrolytes particles in cathode composites facilitate the formation of a percolated Li^+-conduction network and can increase the effective conductivity of the composite. However, only a few methods can achieve the synthesis of SE with <200 nm particle size.[47,48] The particle size of ball-milled $Li_{0.8}ZrCl_4(SO_4)_{0.4}$ is ∼200 nm, as shown in Figure 4a, which is favorable for composite cathode fabrication. EDS mapping shows the homogeneous distribution of Zr, S, and Cl (Figure 4b). The homogeneously distributed S further confirms the distribution of SO_4^{2-} in the amorphous SE. The particles of amorphous $Li_{0.8}ZrCl_4(SO_4)_{0.4}$ are predominantly well-dispersed, as demonstrated in Figure S6. As a comparison, BM-Li_2ZrCl_6 has a larger particle size and forms agglomerates, as indicated in Figures 4c and S7, which is common in other halide electrolytes, like Li_3InCl_6 and Li_3ScCl_6. The deformability of solid electrolytes is critical for achieving the dense stacking of SE separators and ensuring intimate solid–solid contact between the cathode and SEs. To evaluate this property of amorphous $Li_{0.8}ZrCl_4(SO_4)_{0.4}$, pellets of this material and a reference BM-Li_2ZrCl_6 were pressed under the same pressure of 243 MPa. Their surface morphologies were examined using SEM at two magnifications (Figure 4d,e). While the BM-Li_2ZrCl_6 pellet appears relatively compact, it contains numerous pores and cracks. In contrast, the amorphous $Li_{0.8}ZrCl_4(SO_4)_{0.4}$ pellet exhibits a much smoother and denser surface, indicating superior deformability and densification under pressure. The elastic modulus and hardness of amorphous $Li_{0.8}ZrCl_4(SO_4)_{0.4}$ measured by nanoindentation (Figure S8) are 9.55 GPa and 0.35 GPa, respectively, further supporting its good deformability.

The performance of amorphous $Li_{0.8}ZrCl_4(SO_4)_{0.4}$ was evaluated in ASSBs using uncoated LCO and $LiNi_{0.8}Mn_{0.1}Co_{0.1}O_2$ (NMC811) as positive electrodes. Figure 5a presents the schematic configuration of the assembled ASSBs. Given that the reduction potential of ball-milled Li_2ZrCl_6 is reported to be approximately 1.8 V vs Li/Li^+,[49,50] bilayer solid electrolytes consisting of Li_6PS_5Cl (LPSCl) and either amorphous $Li_{0.8}ZrCl_4(SO_4)_{0.4}$ or BM-Li_2ZrCl_6 were used as separators.[51] Figure 5b,c compares the electrochemical performance of ASSBs with LCO cathodes, using either amorphous $Li_{0.8}ZrCl_4(SO_4)_{0.4}$ or BM-Li_2ZrCl_6 as the separator. The cell with amorphous $Li_{0.8}ZrCl_4(SO_4)_{0.4}$ demonstrates a high initial discharge capacity 144 mAh g^{-1} and a high initial Coulombic efficiency of 95.4% at 0.1 C, outperforming the cell with BM-Li_2ZrCl_6 (139 mAh g^{-1} and 88.4%). The higher initial Coulombic efficiency and enhanced cycling stability (Figures S10 and S11) suggest reduced side reactions and improved compatibility between amorphous $Li_{0.8}ZrCl_4(SO_4)_{0.4}$ and LCO. Furthermore, the amorphous $Li_{0.8}ZrCl_4(SO_4)_{0.4}$-based cell exhibits superior rate performance, likely due to its higher ionic conductivity and enhanced deformability, which facilitate a more efficient percolated ionic conduction network. Specifically, it delivers 113.9 and 76.8 mAh g^{-1} at rates of 1 C and 2 C, respectively, while the BM-Li_2ZrCl_6-based cell only achieves 75.0 and 21.1 mAh g^{-1}, respectively.

The performance of ASSBs using NMC811 as the active material and amorphous $Li_{0.8}ZrCl_4(SO_4)_{0.4}$ as the separator

https://doi.org/10.1021/acsenergylett.6c01352
ACS Energy Lett. 2026, 11, 5591−5600

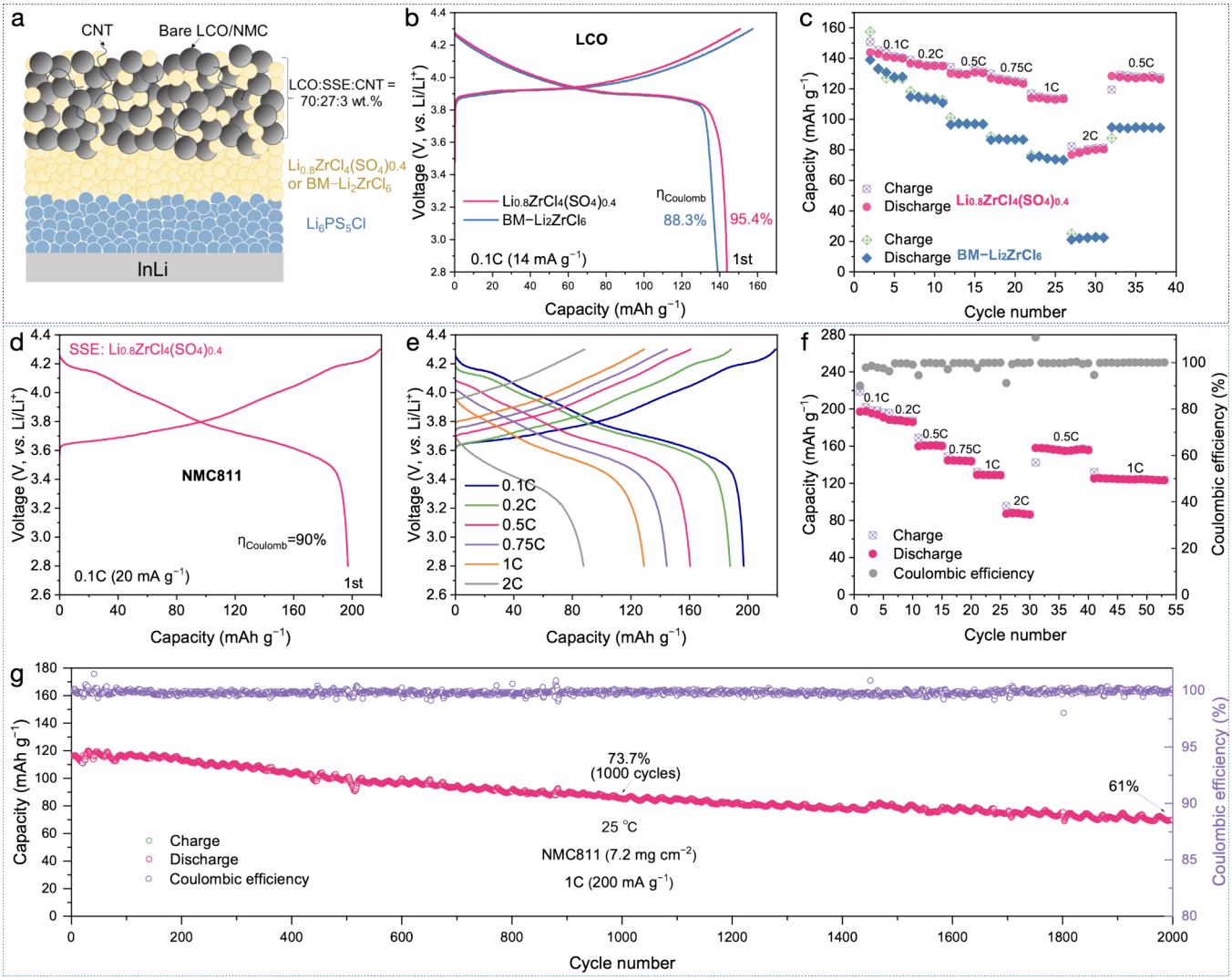

Figure 5. (a) Schematic graph of the all-solid-state batteries (ASSBs) using bilayer solid electrolytes. LCO and NMC 811 are used as active materials in Figure b,c and Figure d–g, respectively. All ASSBs were tested at 25 °C and 20 MPa within a voltage range of 2.8–4.3 V vs Li/Li^+. (b) First-cycle charge–discharge voltage profiles at 0.1 C (14 mA g^{-1}) for ASSBs using Li_2ZrCl_6 or $Li_{0.8}ZrCl_4(SO_4)_{0.4}$ as solid electrolytes. (c) Rate capability of ASSBs employing Li_2ZrCl_6 or $Li_{0.8}ZrCl_4(SO_4)_{0.4}$ as solid electrolytes. (d) First-cycle charge–discharge curves at 0.1 C (20 mA g^{-1}) for ASSBs with $Li_{0.8}ZrCl_4(SO_4)_{0.4}$ as the solid electrolyte and NMC811 as the active material. (e, f) Initial charge–discharge curves of ASSB with $Li_{0.8}ZrCl_4(SO_4)_{0.4}$ as the solid electrolyte at various rates and corresponding rate performances at 0.1, 0.2, 0.5, 0.75, 1, and 2 C. (g) Cycling performance and coulombic efficiency under 1 C.

was also assessed. As shown in Figure 5d–f, the LiIn|LPSCl|amorphous $Li_{0.8}ZrCl_4(SO_4)_{0.4}$|NMC811 cell delivers an initial discharge capacity of 197.1 mAh g^{-1} with a Coulombic efficiency of 90% at 0.1 C and 25 °C. It also demonstrates excellent rate capability, delivering 188.5, 159.8, 144.6, 129.0, and 87.1 mAh g^{-1} at rates of 0.2, 0.5, 0.75, 1, and 2 C, respectively. The cell exhibits cycling stability comparable to that reported for halide-based all-solid-state batteries in the literature (Table S8). As shown in Figure 5g, it retains 61% of its initial capacity after 2000 cycles at 1 C under a stacking pressure of 20 MPa, with an average Coulombic efficiency of 99.75%.

In summary, a series of cost-effective amorphous $Li_{2x}ZrCl_4(SO_4)_x$ solid electrolytes were synthesized using a mechano chemical method. Synchrotron XRD, PDF, and XAS analyses revealed that amorphous $Li_{0.8}ZrCl_4(SO_4)_{0.4}$ and $LiZrCl_4(SO_4)_{0.5}$ possess medium-range order resembling those of their annealed counterparts, which crystallize in $C2/m$ and $P\bar{3}m1$ space groups, respectively. The distinct medium-range order leads to differences in ionic conductivity, highlighting the importance of tuning the local structure of amorphous electrolytes to optimize Li^+ transport. Amorphous $Li_{0.8}ZrCl_4(SO_4)_{0.4}$ combines fast local Li^+ diffusion enabled by the retained medium-range ordering with reduced grain boundary resistance due to its long-range disorder, thus achieving an ionic conductivity of 1.86 mS cm^{-1} at 25 °C. In addition, it also offers a low estimated cost of \$21 kg^{-1} and high oxidative stability up to 4.5 V vs Li/Li^+. As a result, it demonstrates satisfactory electrochemical performance in ASSBs with uncoated LCO or NMC811. This study provides a design strategy for

https://doi.org/10.1021/acsenergylett.6c01352
ACS Energy Lett. 2026, 11, 5591−5600

low-cost, high-performance amorphous solid electrolytes and reveals medium-range ordering as a key factor governing ionic conductivity in amorphous SEs.

■ ASSOCIATED CONTENT

Supporting Information

The Supporting Information is available free of charge at https://pubs.acs.org/doi/10.1021/acsenergylett.6c01352.

Additional results about materials characterization (laboratory XRD, TEM, EXAFS refinement, SEM, nanoindentation measurements, and electronic conductivity tests), cost estimation, and electrochemical performance evaluation (DOCX)

■ AUTHOR INFORMATION

Corresponding Authors

Yuanzhi Tang – *School of Earth and Atmospheric Sciences, Georgia Institute of Technology, Atlanta, Georgia 30332, United States;* orcid.org/0000-0002-7741-8646; Email: yuanzhi.tang@eas.gatech.edu

Hailong Chen – *The Woodruff School of Mechanical Engineering, Georgia Institute of Technology, Atlanta, Georgia 30332, United States;* orcid.org/0000-0001-8283-2860; Email: hailong.chen@me.gatech.edu

Authors

Guangxing Zhang – *The Woodruff School of Mechanical Engineering, Georgia Institute of Technology, Atlanta, Georgia 30332, United States*

Zhantao Liu – *The Woodruff School of Mechanical Engineering, Georgia Institute of Technology, Atlanta, Georgia 30332, United States;* orcid.org/0000-0003-1072-6457

Yifan Ma – *The Woodruff School of Mechanical Engineering, Georgia Institute of Technology, Atlanta, Georgia 30332, United States*

Jakub Pepas – *The Woodruff School of Mechanical Engineering, Georgia Institute of Technology, Atlanta, Georgia 30332, United States; School of Materials Science and Engineering, Georgia Institute of Technology, Atlanta, Georgia 30332, United States*

Hang Xu – *School of Earth and Atmospheric Sciences, Georgia Institute of Technology, Atlanta, Georgia 30332, United States*

Rui Cai – *School of Earth and Atmospheric Sciences, Georgia Institute of Technology, Atlanta, Georgia 30332, United States*

Shuman Xia – *The Woodruff School of Mechanical Engineering, Georgia Institute of Technology, Atlanta, Georgia 30332, United States*

Yong Ding – *School of Materials Science and Engineering, Georgia Institute of Technology, Atlanta, Georgia 30332, United States*

Jianming Bai – *National Synchrotron Light Source II, Brookhaven National Laboratory, Upton, New York 11973, United States;* orcid.org/0000-0002-0575-2987

Hui Zhong – *National Synchrotron Light Source II, Brookhaven National Laboratory, Upton, New York 11973, United States*

Complete contact information is available at: https://pubs.acs.org/doi/10.1021/acsenergylett.6c01352

Notes

The authors declare the following competing financial interest(s): The authors declare that the work described in this manuscript is related to a submitted technical disclosure that may form the basis of future intellectual property.

■ ACKNOWLEDGMENTS

This work was financially supported by NSF project 2004878 and NSF project 2108688. H.X., R. C., and Y.T. acknowledge the financial support by NSF project 2327660. This research used resources at Brookhaven National Laboratory, which is supported by the U.S. Department of Energy (DOE) Office of Science, through the general user programs. We thank the beamline scientists at 5-BM-D of the Advanced Photon Source (APS) for their assistance with data collection. APS is a U.S. Department of Energy Office of Science User Facility operated by Argonne National Laboratory under Contract No. DE-AC02-06CH11357.

■ REFERENCES

(1) Famprikis, T.; Canepa, P.; Dawson, J. A.; Islam, M. S.; Masquelier, C. Fundamentals of Inorganic Solid-State Electrolytes for Batteries. *Nat. Mater.* **2019**, *18* (12), 1278–1291.

(2) Manthiram, A.; Yu, X.; Wang, S. Lithium Battery Chemistries Enabled by Solid-State Electrolytes. *Nat. Rev. Mater.* **2017**, *2* (4), 16103.

(3) Janek, J.; Zeier, W. G. Challenges in Speeding up Solid-State Battery Development. *Nat. Energy* **2023**, *8* (3), 230–240.

(4) Xiao, Y.; Wang, Y.; Bo, S.-H.; Kim, J. C.; Miara, L. J.; Ceder, G. Understanding Interface Stability in Solid-State Batteries. *Nat. Rev. Mater.* **2020**, *5* (2), 105–126.

(5) Kraft, M. A.; Culver, S. P.; Calderon, M.; Böcher, F.; Krauskopf, T.; Senyshyn, A.; Dietrich, C.; Zevalkink, A.; Janek, J.; Zeier, W. G. Influence of Lattice Polarizability on the Ionic Conductivity in the Lithium Superionic Argyrodites Li_6PS_5X (X = Cl, Br, I). *J. Am. Chem. Soc.* **2017**, *139* (31), 10909–10918.

(6) Kato, Y.; Hori, S.; Saito, T.; Suzuki, K.; Hirayama, M.; Mitsui, A.; Yonemura, M.; Iba, H.; Kanno, R. High-Power All-Solid-State Batteries Using Sulfide Superionic Conductors. *Nat. Energy* **2016**, *1*, 16030.

(7) Xiong, S.; Liu, Z.; Yang, L.; Ma, Y.; Xu, W.; Bai, J.; Chen, H. Anion and Cation Co-Doping of Na_4SnS_4 as Sodium Superionic Conductors. *Mater. Today Phys.* **2020**, *15*, 100281.

(8) Liu, Z.; Zinkevich, T.; Indris, S.; He, X.; Liu, J.; Xu, W.; Bai, J.; Xiong, S.; Mo, Y.; Chen, H. $Li_{15}P_4S_{16}Cl_3$, a Lithium Chlorothiophosphate as a Solid-State Ionic Conductor. *Inorg. Chem.* **2020**, *59* (1), 226–234.

(9) Han, X.; Gong, Y.; Fu, K. (K.); He, X.; Hitz, G. T.; Dai, J.; Pearse, A.; Liu, B.; Wang, H.; Rubloff, G.; Mo, Y.; Thangadurai, V.; Wachsman, E. D.; Hu, L. Negating Interfacial Impedance in Garnet-Based Solid-State Li Metal Batteries. *Nat. Mater.* **2017**, *16* (5), 572–579.

(10) Xiong, S.; He, X.; Han, A.; Liu, Z.; Ren, Z.; McElhenny, B.; Nolan, A. M.; Chen, S.; Mo, Y.; Chen, H. Computation-Guided Design of $LiTaSiO_5$, a New Lithium Ionic Conductor with Sphene Structure. *Adv. Energy Mater.* **2019**, *9* (22), 1803821.

(11) Wang, S.; Bai, Q.; Nolan, A. M.; Liu, Y.; Gong, S.; Sun, Q.; Mo, Y. Lithium Chlorides and Bromides as Promising Solid-State Chemistries for Fast Ion Conductors with Good Electrochemical Stability. *Angew. Chem., Int. Ed.* **2019**, *58* (24), 8039–8043.

(12) Liu, Z.; Ma, S.; Liu, J.; Xiong, S.; Ma, Y.; Chen, H. High Ionic Conductivity Achieved in $Li_3Y(Br_3Cl_3)$ Mixed Halide Solid Electrolyte via Promoted Diffusion Pathways and Enhanced Grain Boundary. *ACS Energy Lett.* **2021**, *6* (1), 298–304.

(13) Liu, Z.; Chien, P.-H.; Wang, S.; Song, S.; Lu, M.; Chen, S.; Xia, S.; Liu, J.; Mo, Y.; Chen, H. Tuning Collective Anion Motion Enables Superionic Conductivity in Solid-State Halide Electrolytes. *Nat. Chem.* **2024**, *16* (10), 1584–1591.

(14) Li, X.; Liang, J.; Yang, X.; Adair, K. R.; Wang, C.; Zhao, F.; Sun, X. Progress and Perspectives on Halide Lithium Conductors for All-Solid-State Lithium Batteries. *Energy Environ. Sci.* **2020**, *13* (5), 1429–1461.
(15) Kwak, H.; Wang, S.; Park, J.; Liu, Y.; Kim, K. T.; Choi, Y.; Mo, Y.; Jung, Y. S. Emerging Halide Superionic Conductors for All-Solid-State Batteries: Design, Synthesis, and Practical Applications. *ACS Energy Lett.* **2022**, *7* (5), 1776–1805.
(16) Asano, T.; Sakai, A.; Ouchi, S.; Sakaida, M.; Miyazaki, A.; Hasegawa, S. Solid Halide Electrolytes with High Lithium-Ion Conductivity for Application in 4 V Class Bulk-Type All-Solid-State Batteries. *Adv. Mater.* **2018**, *30* (44), 1803075.
(17) Li, X.; Liang, J.; Luo, J.; Banis, M. N.; Wang, C.; Li, W.; Deng, S.; Yu, C.; Zhao, F.; Hu, Y.; Sham, T.-K.; Zhang, L.; Zhao, S.; Lu, S.; Huang, H.; Li, R.; Adair, K. R.; Sun, X. Air-Stable Li_3InCl_6 Electrolyte with High Voltage Compatibility for All-Solid-State Batteries. *Energy Environ. Sci.* **2019**, *12* (9), 2665–2671.
(18) Liang, J.; Li, X.; Wang, S.; Adair, K. R.; Li, W.; Zhao, Y.; Wang, C.; Hu, Y.; Zhang, L.; Zhao, S.; Lu, S.; Huang, H.; Li, R.; Mo, Y.; Sun, X. Site-Occupation-Tuned Superionic Li_xScCl_{3+x} Halide Solid Electrolytes for All-Solid-State Batteries. *J. Am. Chem. Soc.* **2020**, *142* (15), 7012–7022.
(19) Zhou, L.; Zuo, T.-T.; Kwok, C. Y.; Kim, S. Y.; Assoud, A.; Zhang, Q.; Janek, J.; Nazar, L. F. High Areal Capacity, Long Cycle Life 4 V Ceramic All-Solid-State Li-Ion Batteries Enabled by Chloride Solid Electrolytes. *Nat. Energy* **2022**, *7* (1), 83–93.
(20) Tanaka, Y.; Ueno, K.; Mizuno, K.; Takeuchi, K.; Asano, T.; Sakai, A. New Oxyhalide Solid Electrolytes with High Lithium Ionic Conductivity >10 mS cm^{-1} for All-Solid-State Batteries. *Angew. Chem., Int. Ed.* **2023**, *62*, e202217581.
(21) Yin, Y.-C.; Yang, J.-T.; Luo, J.-D.; Lu, G.-X.; Huang, Z.; Wang, J.-P.; Li, P.; Li, F.; Wu, Y.-C.; Tian, T.; Meng, Y.-F.; Mo, H.-S.; Song, Y.-H.; Yang, J.-N.; Feng, L.-Z.; Ma, T.; Wen, W.; Gong, K.; Wang, L.-J.; Ju, H.-X.; Xiao, Y.; Li, Z.; Tao, X.; Yao, H.-B. A $LaCl_3$-Based Lithium Superionic Conductor Compatible with Lithium Metal. *Nature* **2023**, *616* (7955), 77–83.
(22) Schnell, J.; Knörzer, H.; Imbsweiler, A. J.; Reinhart, G. Solid versus Liquid—A Bottom-Up Calculation Model to Analyze the Manufacturing Cost of Future High-Energy Batteries. *Energy Technol.* **2020**, *8* (3), 1901237.
(23) Wang, K.; Ren, Q.; Gu, Z.; Duan, C.; Wang, J.; Zhu, F.; Fu, Y.; Hao, J.; Zhu, J.; He, L.; Wang, C.-W.; Lu, Y.; Ma, J.; Ma, C. A Cost-Effective and Humidity-Tolerant Chloride Solid Electrolyte for Lithium Batteries. *Nat. Commun.* **2021**, *12* (1), 4410.
(24) Kwak, H.; Han, D.; Lyoo, J.; Park, J.; Jung, S. H.; Han, Y.; Kwon, G.; Kim, H.; Hong, S.-T.; Nam, K.-W.; Jung, Y. S. New Cost-Effective Halide Solid Electrolytes for All-Solid-State Batteries: Mechanochemically Prepared Fe^{3+}-Substituted Li_2ZrCl_6. *Adv. Energy Mater.* **2021**, *11* (12), 2003190.
(25) Kwak, H.; Kim, J.-S.; Han, D.; Kim, J. S.; Park, J.; Kwon, G.; Bak, S.-M.; Heo, U.; Park, C.; Lee, H.-W.; Nam, K.-W.; Seo, D.-H.; Jung, Y. S. Boosting the Interfacial Superionic Conduction of Halide Solid Electrolytes for All-Solid-State Batteries. *Nat. Commun.* **2023**, *14* (1), 2459.
(26) Wang, J.; Chen, F.; Ma, C. Alternate Crystal Structure Achieving Ionic Conductivity above 1 mS cm^{-1} in Cost-Effective Zr-Based Chloride Solid Electrolytes. *Nano Lett.* **2023**, *23* (13), 6081–6087.
(27) Zhang, S.; Zhao, F.; Chang, L.-Y.; Chuang, Y.-C.; Zhang, Z.; Zhu, Y.; Hao, X.; Fu, J.; Chen, J.; Luo, J.; Li, M.; Gao, Y.; Huang, Y.; Sham, T.-K.; Gu, M. D.; Zhang, Y.; King, G.; Sun, X. Amorphous Oxyhalide Matters for Achieving Lithium Superionic Conduction. *J. Am. Chem. Soc.* **2024**, *146* (5), 2977–2985.
(28) Ishiguro, Y.; Ueno, K.; Nishimura, S.; Iida, G.; Igarashib, Y. TaCl5-Glassified Ultrafast Lithium Ion-Conductive Halide Electrolytes for High-Performance All-Solid-State Lithium Batteries. *Chem. Lett.* **2023**, *52*, 237–241.
(29) Li, F.; Cheng, X.; Lu, G.; Yin, Y.-C.; Wu, Y.-C.; Pan, R.; Luo, J.-D.; Huang, F.; Feng, L.-Z.; Lu, L.-L.; Ma, T.; Zheng, L.; Jiao, S.; Cao, R.; Liu, Z.-P.; Zhou, H.; Tao, X.; Shang, C.; Yao, H.-B. Amorphous Chloride Solid Electrolytes with High Li-Ion Conductivity for Stable Cycling of All-Solid-State High-Nickel Cathodes. *J. Am. Chem. Soc.* **2023**, *145* (50), 27774–27787.
(30) Ridley, P.; Nguyen, L. H. B.; Sebti, E.; Han, B.; Duong, G.; Chen, Y.-T.; Sayahpour, B.; Cronk, A.; Deysher, G.; Ham, S.-Y.; Oh, J. A. S.; Wu, E. A.; Tan, D. H. S.; Doux, J.-M.; Clément, R.; Jang, J.; Meng, Y. S. Amorphous and Nanocrystalline Halide Solid Electrolytes with Enhanced Sodium-Ion Conductivity. *Matter* **2024**, *7* (2), 485–499.
(31) Song, Y.; Xue, S.; Xu, Z.; Fang, J.; Zhan, Z.; Wang, Y.-H.; Chen, C.; Li, S.; Liu, T.; Yang, Y.; Yang, L.; Pan, F. 1D $ZrCl_4$ Matrices for Enhanced Ion Transport in Glassy Chloride Electrolytes. *Adv. Energy Mater.* **2025**, *15*, 2500913.
(32) Inoishi, A.; Nojima, A.; Tanaka, M.; Suyama, M.; Okada, S.; Sakaebe, H. Superionic Conductivity in Sodium Zirconium Chloride-Based Compounds. *Chem. – Eur. J.* **2023**, *29* (52), e202301586.
(33) Yue, J.; Zhang, S.; Wang, X.; Fu, J.; Xu, Y.; Weng, S.; Zhu, Y.; Zhao, C.; Zheng, M.; Wang, Y.; Zhu, X.; Wu, H.; Wang, G.; Xia, Y.; Cao, M.; Jing, Q.; Wang, X.; Xia, W.; Liang, J.; Sun, X.; Li, X. Universal Superionic Conduction via Solid Dissociation of Salts in van Der Waals Materials. *Nat. Energy* **2025**, *10*, 1237–1250.
(34) Hu, Y.; Fu, J.; Xu, J.; Luo, J.; Zhao, F.; Su, H.; Liu, Y.; Lin, X.; Li, W.; Kim, J. T.; Hao, X.; Yao, X.; Sun, Y.; Ma, J.; Ren, H.; Yang, M.; Huang, Y.; Sun, X. Superionic Amorphous $NaTaCl_6$ Halide Electrolyte for Highly Reversible All-Solid-State Na-Ion Batteries. *Matter* **2024**, *7*, 1018–1034.
(35) Chandra, A.; Bhatt, A.; Chandra, A. Ion Conduction in Superionic Glassy Electrolytes: An Overview. *J. Mater. Sci. Technol.* **2013**, *29* (3), 193–208.
(36) Tatsumisago, M.; Hayashi, A. Superionic Glasses and Glass–Ceramics in the Li_2S–P_2S_5 System for All-Solid-State Lithium Secondary Batteries. *Solid State Ionics* **2012**, *225*, 342–345.
(37) Elliott, S. R. Medium-Range Structural Order in Covalent Amorphous Solids. *Nature* **1991**, *354* (6353), 445–452.
(38) Yang, Y.; Zhou, J.; Zhu, F.; Yuan, Y.; Chang, D. J.; Kim, D. S.; Pham, M.; Rana, A.; Tian, X.; Yao, Y.; Osher, S. J.; Schmid, A. K.; Hu, L.; Ercius, P.; Miao, J. Determining the Three-Dimensional Atomic Structure of an Amorphous Solid. *Nature* **2021**, *592* (7852), 60–64.
(39) Mavračić, J.; Mocanu, F. C.; Deringer, V. L.; Csányi, G.; Elliott, S. R. Similarity Between Amorphous and Crystalline Phases: The Case of TiO_2. *J. Phys. Chem. Lett.* **2018**, *9* (11), 2985–2990.
(40) Momma, K.; Izumi, F. *VESTA 3* for Three-Dimensional Visualization of Crystal, Volumetric and Morphology Data. *J. Appl. Crystallogr.* **2011**, *44* (6), 1272–1276.
(41) Reimer, J.; Steele-MacInnis, M.; Wambach, J. M.; Vogel, F. Ion Association in Hydrothermal Sodium Sulfate Solutions Studied by Modulated FT-IR-Raman Spectroscopy and Molecular Dynamics. *J. Phys. Chem. B* **2015**, *119* (30), 9847–9857.
(42) Almond, D. P.; West, A. R. Anomalous Conductivity Prefactors in Fast Ion Conductors. *Nature* **1983**, *306* (5942), 456–457.
(43) Wang, Y.; Richards, W. D.; Ong, S. P.; Miara, L. J.; Kim, J. C.; Mo, Y.; Ceder, G. Design Principles for Solid-State Lithium Superionic Conductors. *Nat. Mater.* **2015**, *14* (10), 1026–1031.
(44) Wang, J.; Hsu, C.-S.; Wu, T.-S.; Chan, T.-S.; Suen, N.-T.; Lee, J.-F.; Chen, H. M. In Situ X-Ray Spectroscopies beyond Conventional X-Ray Absorption Spectroscopy on Deciphering Dynamic Configuration of Electrocatalysts. *Nat. Commun.* **2023**, *14* (1), 6576.
(45) Rehr, J. J.; Albers, R. C. Theoretical Approaches to X-Ray Absorption Fine Structure. *Rev. Mod. Phys.* **2000**, *72* (3), 621–654.
(46) Shi, T.; Tu, Q.; Tian, Y.; Xiao, Y.; Miara, L. J.; Kononova, O.; Ceder, G. High Active Material Loading in All-Solid-State Battery Electrode via Particle Size Optimization. *Adv. Energy Mater.* **2020**, *10* (1), 1902881.
(47) Ma, T.; Wang, Z.; Wu, D.; Lu, P.; Zhu, X.; Yang, M.; Peng, J.; Chen, L.; Li, H.; Wu, F. High-Areal-Capacity and Long-Cycle-Life All-Solid-State Battery Enabled by Freeze Drying Technology. *Energy Environ. Sci.* **2023**, *16*, 2142.

https://doi.org/10.1021/acsenergylett.6c01352
ACS Energy Lett. 2026, 11, 5591–5600

(48) Wang, C.; Liang, J.; Luo, J.; Liu, J.; Li, X.; Zhao, F.; Li, R.; Huang, H.; Zhao, S.; Zhang, L.; Wang, J.; Sun, X. A Universal Wet-Chemistry Synthesis of Solid-State Halide Electrolytes for All-Solid-State Lithium-Metal Batteries. *Sci. Adv.* **2021**, *7* (37), eabh1896.
(49) Luo, X.; Zhong, Y.; Wang, X.; Xia, X.; Gu, C.; Tu, J. Ionic Conductivity Enhancement of Li_2ZrCl_6 Halide Electrolytes via Mechanochemical Synthesis for All-Solid-State Lithium–Metal Batteries. *ACS Appl. Mater. Interfaces* **2022**, *14* (44), 49839–49846.
(50) Shao, Q.; Yan, C.; Gao, M.; Du, W.; Chen, J.; Yang, Y.; Gan, J.; Wu, Z.; Sun, W.; Jiang, Y.; Liu, Y.; Gao, M.; Pan, H. New Insights into the Effects of Zr Substitution and Carbon Additive on $Li_{3-x}Er_{1-x}Zr_xCl_6$ Halide Solid Electrolytes. *ACS Appl. Mater. Interfaces* **2022**, *14* (6), 8095–8105.
(51) Panchal, A. A.; Pennebaker, T. N. T.; Sebti, E.; Li, Y.; Li, Y.; Clément, R. J.; Canepa, P. Compatibility of Halide Bilayer Separators for All-Solid-State Batteries. *ACS Energy Lett.* **2024**, *9* (12), 5935–5944.

https://doi.org/10.1021/acsenergylett.6c01352
ACS Energy Lett. 2026, 11, 5591−5600